Phosphate Elimination and Recovery Lightweight (PEARL) membrane: A sustainable environmental remediation approach

Stephanie M. Ribet[a], Benjamin Shindel[a], Roberto dos Reis[a,b], Vikas Nandwana[a], and Vinayak P. Dravid[a,b,c,1]

[a]Department of Materials Science and Engineering, Northwestern University, Evanston, IL 60208; [b]The Northwestern University Atomic and Nanoscale Characterization Experimental Center, Northwestern University, Evanston, IL 60208; and [c]International Institute of Nanotechnology, Northwestern University, Evanston, IL 60208

Edited by Alexis T. Bell, University of California, Berkeley, CA, and approved April 26, 2021 (received for review February 8, 2021)

Aqueous phosphate pollution can dramatically impact ecosystems, introducing a variety of environmental, economic, and public health problems. While novel remediation tactics based on nanoparticle binding have shown considerable promise in nutrient recovery from water, they are challenging to deploy at scale. To bridge the gap between the laboratory-scale nature of these nanostructure solutions and the practical benchmarks for deploying an environmental remediation tool, we have developed a nanocomposite material. Here, an economical, readily available, porous substrate is dip coated using scalable, water-based processes with a slurry of nanostructures. These nanomaterials have tailored affinity for specific adsorption of pollutants. Our Phosphate Elimination and Recovery Lightweight (PEARL) membrane can selectively sequester up to 99% of phosphate ions from polluted waters at environmentally relevant concentrations. Moreover, mild tuning of pH promotes at will adsorption and desorption of nutrients. This timed release allows for phosphate recovery and reuse of the PEARL membrane repeatedly for numerous cycles. We combine correlative microscopy and spectroscopy techniques to characterize the complex microstructure of the PEARL membrane and to unravel the mechanism of phosphate sorption. More broadly, through the example of phosphate pollution, this work describes a platform membrane approach based on nanostructures with specific affinity coated on a porous structure. Such a strategy can be tuned to address other environmental remediation challenges through the incorporation of other nanomaterials.

eutrophication | nutrient pollution | nanotechnology | electron microscopy | adsorption

In many ecosystems, phosphates and nitrates are the limiting reactants for growth, so small changes in ion concentrations can have profound effects. Through a variety of human activities, phosphates are being extracted for use and flushed away, releasing excess nutrients into ecosystems (1). This process of nutrient buildup in natural bodies of water, which is referred to as anthropogenic hypereutrophication, causes a variety of economic, environmental, and public health consequences around the globe due to the sensitivity of systems to these essential anions (2–5).

Although a myriad of municipal and industrial processes contributes to hypereutrophication, nutrient pollution is most often associated with agriculture (5). Phosphates and nitrates are essential for plant growth, but when added to fertilizer at an industrial scale, large volumes of unused nutrients run off into natural bodies of water. The release of excess phosphates and nitrates makes blue-green algae more liable to bloom. In addition to blocking sunlight and producing toxins, these algae lead to the proliferation of bacteria following the end of their life cycle. As these bacteria break down dead matter, they consume oxygen, leading to hypoxia and prompting a positive feedback loop (6).

Natural systems are incredibly sensitive to these nutrients, as pollutant concentrations as low as single-digit micrograms of phosphorus per liter (mg of P/L) can alter a biosphere. Depending on the ecosystem's chemistry, either phosphorus or nitrogen is the most troublesome anion (7, 8). This problem is projected to get worse with climate change, contributing to the call to action to remediate both phosphates and nitrates with selective, sustainable, cost-effective methods (9, 10). We demonstrate an efficient strategy toward recovering dissolved phosphates that has the potential to meet practical considerations demanded by environmental remediation challenges.

Challenge of Phosphate Pollution: An Unmet Critical Need

Water treatment plants remove phosphates through a combination of chemical, physical, and biological methods, which traditionally have focused on phosphate elimination rather than recovery. Phosphate fertilizers are usually produced from phosphate rock, a nonrenewable natural resource of limited supply (10, 11).

Chemical methods, such as precipitation with metal salt, work only at high concentrations, create secondary pollution, and remove but do not recover phosphates (12). Some facilities have demonstrated phosphate recovery through precipitation of

Significance

The large scale of pollution requires solutions that are efficient and effective while meeting economic and engineering considerations. We report the Phosphate Elimination and Recovery Lightweight (PEARL) membrane, a nanocomposite that can be used to selectively and repeatably recover phosphate at will from contaminated waters. The PEARL membrane is made through a scalable, aqueous process. An inexpensive porous structure is coated with a slurry of nanostructures tailored for selective sorption of pollutants. Characterization of the PEARL membrane provides compelling scientific insights into its complex architecture and its binding of phosphate. The PEARL membrane approach is potentially general and versatile such that it can be tuned to remediate other contaminants with the same core principles of performance, scalability, reusability, and cost-effectiveness.

Author contributions: S.M.R., B.S., R.d.R., V.N., and V.P.D. designed research, performed research, contributed new reagents/analytic tools, analyzed data, and wrote the paper.

Competing interest statement: A provisional patent related to this research has been filed.

This article is a PNAS Direct Submission.

Published under the PNAS license.

[1]To whom correspondence may be addressed. Email: v-dravid@northwestern.edu.

This article contains supporting information online at https://www.pnas.org/lookup/suppl/doi:10.1073/pnas.2102583118/-/DCSupplemental.

Published June 4, 2021.

Downloaded by guest on January 7, 2022

struvite, a fertilizer, but these methods operate best at concentrations exceeding 50 mg of P/L (12). Physical methods, such as ion exchanges and membranes, can be expensive to implement and require additional chemicals for membrane regeneration (12). In biological processes, phosphate-accumulating organisms are used to remove anions, but these methods require the addition of organic carbon and result in the creation of waste sludge. New processes are being employed to recover phosphate from this biomass (11, 13). Recent pilot studies have shown algae or other plants themselves can be grown in a controlled manner to sequester nutrients while removing atmospheric carbon dioxide and creating a biomass with other industrial applications (13, 14). These concepts can be combined to form a constructed wetland approach to remediate water (15). Although there are many promising removal methods, there still lacks an efficient, scalable approach for phosphate recovery, especially in the critical concentration range of 1 to 10 mg of P/L.

A Nanotechnology-Based Solution: Advantages and Opportunities for Improvement

The tunability of nanoparticles, as well as their high surface area to volume ratio, makes nanostructured media a promising and novel approach to both nutrient remediation and recovery of other dissolved pollutants (16–18). However, there are several practical drawbacks to using many nanomaterials for large-scale phosphate remediation. In order to treat a problem of this magnitude, the solution must be easily manufacturable, which challenges a number of complex nanostructures (19–21).

The proposed use of iron oxide nanoparticles for phosphate remediation begins to address some practical environmental stewardship considerations. These structures are scalable and have shown incredible promise for phosphate sequestration (22–26). Even with these cost-effective and easily manufacturable nanomaterials, it can be challenging to use them in practice. Studies rely on centrifugation (22), magnetic fields (23), or fine filters (22, 24–26) to separate the nanoparticles from the aqueous solutions after remediation. These processes sacrifice efficiency and require the introduction of an additional onerous treatment step.

The PEARL Membrane

In order to overcome the challenges with typical nanoparticle remediation strategies, we have developed a platform approach. A hierarchically porous substrate, such as a sponge or membrane, serves to anchor multifunctional nanostructures (MNS) in the form of a thin coating. Thus, an MNS-laden sponge or membrane acts as a carrier to deploy nanostructures for capturing specific analytes or toxins.

This strategy makes efficient use of resources, as even a very thin coating layer (5 to 10 wt %) can transform this cheap, readily available sponge into a targeted sorbent. Moreover, we utilize water-based processes with earth-abundant elements that are compatible with industrial processes, making this an even more appealing approach.

We demonstrated such an architecture with the Oleophilic, Hydrophobic, Magnetic (OHM) sponge, which is used for oil spill remediation (27, 28). For this material, polyurethane was carefully chosen as the backbone due to its intrinsic hydrophobic properties. This sponge was coated with carbon-based substrates and metal oxide nanoparticles that imparted oleophilic/hydrophobic and magnetic character, respectively. In addition to being a remarkably efficient oil remediation tool, the OHM sponge is economic and eco-friendly, making it a promising emerging technology.

A similar approach (Fig. 1) can be employed for targeted recovery of excess dissolved ions, and herein, we demonstrate how our Phosphate Elimination and Recovery Lightweight (PEARL) membrane is used for the capture of nutrients.

Although other nanoparticle composite materials (nanocomposites) have been reported (29, 30), the hydrophilic character and high surface area to volume ratio of cellulose make it especially apt for facilitating phosphate–nanoparticle interactions. Moreover, cellulose is highly versatile, so the PEARL membrane can be deployed in a number of configurations including sorbent pads, booms, and fixed bed reactors.

The PEARL membrane is not only an efficient phosphate sequestration tool, but also, tests have demonstrated that it does so in a selective manner. Because we also observe that the degree of analyte binding is quite tunable, we can use mild conditions for at will adsorption and desorption, which allows for the recovery of phosphate and reuse of the membrane.

There are deliberate and designed similarities between the PEARL membrane and our previously reported material the OHM sponge (27). As a platform technology, we aim to develop a remediation approach that is multiplexed and anchored on key concepts of performance, scalability, reusability, and cost-effectiveness. Other than these core considerations, there is a clear differentiation between the OHM sponge and the PEARL membrane, including hydrophilic/hydrophobic character, use of a carbon-based substrate in addition to the MNS, and mechanism of pollutant sequestration and desorption. Thus, the OHM sponge and PEARL membrane are distinct yet enjoy the core advantages of a flexible and porous membrane coated with tailored nanostructures to create a scalable, cost-effective, and reusable remediation tool, made from earth-abundant and often-discarded precursors.

Moreover, the success of our PEARL membrane as a second construction of this platform has spurred us to continue a similar strategy for remediation of other pollutants, expanding the broader implication of this report. Other nanostructures have been reported for remediation, such as zinc oxide for Zn (II), Cd (II), and Hg (II) remediation (31) and CuO nanostructures for Pb (II) remediation (32), that when decorated

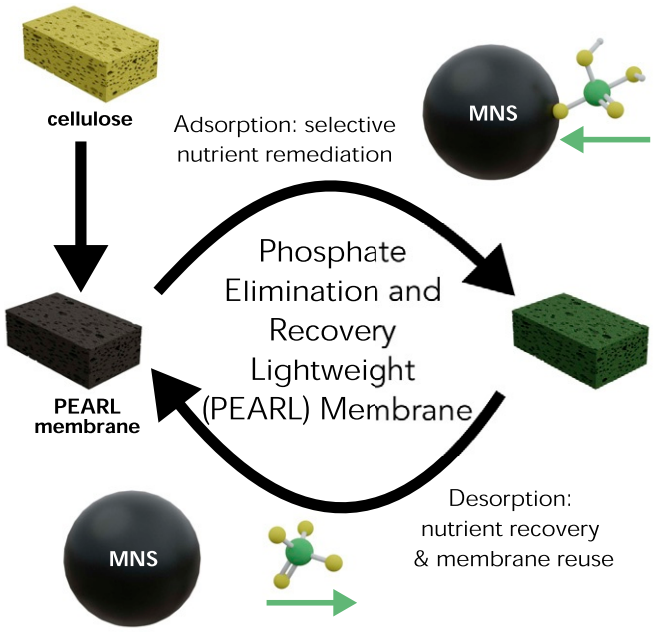


Fig. 1. The PEARL membrane is made by coating cellulose with MNS using a scalable, water-based process. The nanomaterials are tailored for selective phosphate binding. Using mild conditions, the phosphate can be adsorbed and desorbed, allowing for reuse of the PEARL membrane and recovery of anions.

Downloaded by guest on January 7, 2022

on a porous structure would be consistent with our platform membrane approach.

This paper will provide details on the structure of the PEARL membrane, demonstrate its efficacy for phosphate remediation, study the molecular scale nanoparticle–phosphate interactions, and highlight how this approach can be extended to other pollutants.

Results and Discussion

The Architecture of the PEARL Membrane. Like its predecessor the OHM sponge (27, 28), the platform membrane consists of two key components, a membrane and a nanoparticle coating, each of which can be tuned to the specific water remediation challenge. Cellulose was chosen as the platform for the PEARL membrane because of its hydrophilic character, large surface area to volume ratio, and hierarchical structure. These features enable it to facilitate large flow rates and necessary nanoparticle-dissolved pollutant interactions. It is also widely commercially available, biocompatible, and affordable.

Iron oxide nanoparticles have shown promise in phosphate remediation and display many promising qualities that could make them a deployable technology, such as scalability and natural chemical abundance (22–26). This architecture, where the nanostructures are anchored on the cellulose, turns this promising nanostructure into a realizable solution.

Moreover, our synthesis method makes use of scalable, water-based processes using naturally abundant precursors. This facile yet effective dip-coating method is quite tunable, opening up the possibility of introducing other nanostructure on the same structure for targeted recovery of other dissolved analytes.

In order to understand the performance of the membrane, it is important to study the properties of the structure. However, there are significant intrinsic challenges in characterizing such a membrane due to its porous, hierarchical structure and its hybrid composition of soft (cellulose) and hard (iron oxide) structures. Nevertheless, using a correlative microscopy approach, we are able to describe the structure of the PEARL membrane at multiple length scales to help understand its remediation behavior.

As shown in the scanning electron microscopy (SEM) image in Fig. 2*A*, the cellulose exhibits a hierarchical structure with pores at multiple length scales, including at the macro scale, as shown in Fig. 2 *A*, *Inset*. The coating is made of magnetite nanoparticles, whose Fe_3O_4 chemical composition is confirmed by powder X-ray diffraction (*SI Appendix*, Fig. S1). Fig. 2 *B*, *Inset* shows the PEARL membrane, which retains the structure of the cellulose while anchoring the nanostructures.

To better understand the properties of the coating, we employed an ultramicrotome to prepare cross-sections of the sample. The PEARL membrane (Fig. 2*B*) shows expected features: coating, resin, and cellulose. The iron oxide nanoparticle coating is not entirely uniform, but it is possible to see that it is covering most outer surfaces. The cellulose sponge without coating (*SI Appendix*, Fig. S2) imaged in the same mode shows that the coating process modified only the surface of the membrane. Because the molecular scale interactions of the membrane happen at its solid–fluid interface, these scanning electron microscopy images suggest that the nanocoating was successfully applied, as the functional component is present across the entire surface, without intercalating within the membrane.

A multimodal approach was employed to investigate more closely regions with low levels of coating. The bright-field (BF) image (Fig. 2*C*) shows that the nanoparticles on the sponge are approximately 10 nm in diameter. The dark-field (DF) image (Fig. 2*D*) suggests the coating is made of heavy elements. The energy-dispersive X-ray spectroscopy (EDS) map (Fig. 2*E*) confirms as expected that the coating is composed of iron. *SI Appendix*, Fig. S3 shows the full EDS spectra. In this region, the coating is incredibly thin, even on the order of a single nanoparticle.

From our electron microscopy analysis, we observe that there is some degree of agglomeration, which is expected from a scalable coating method that avoids complex processes and toxic chemicals. Nonetheless, areas that appeared dim in other images may in fact have an ultrathin coating contributing to the functional performance of the PEARL membrane.

Thermogravimetric analysis (TGA) and surface area analysis can provide correlative estimates of nanoparticle loading.

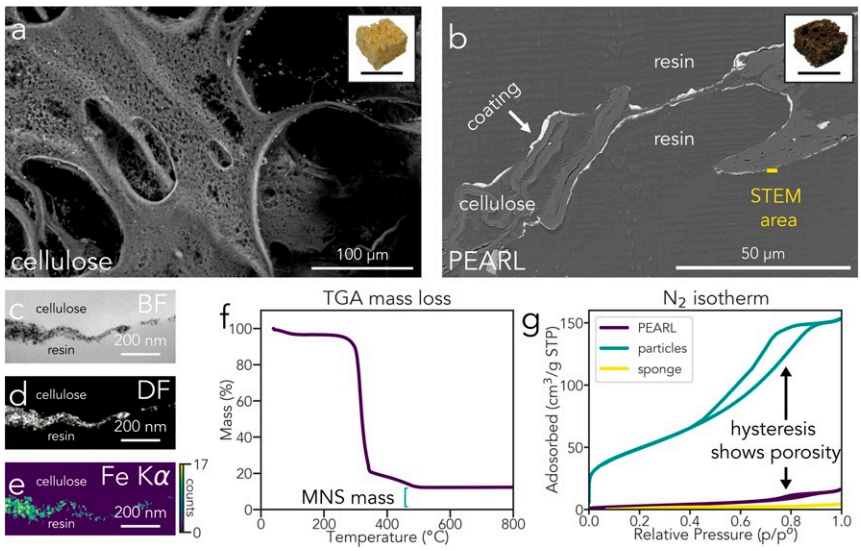


Fig. 2. (*A*) Cellulose imaged at the microscale. *Inset* shows bulk cellulose. (*B*) A scanning electron microscopy image of the cross-section of the PEARL membrane reveals the nature of the coating. *Inset* shows the PEARL membrane. (*C*) BF, (*D*) DF, and (*E*) EDS map from the area marked in yellow in *B* show an ultrathin iron oxide nanoparticle coating. (*F*) TGA quantifies the mass loading of MNS on the PEARL membrane. (*G*) N_2 adsorption isotherm reveals surface area and porosity profile of the PEARL membrane, cellulose, and nanoparticles. (Scale bars: *A*, *Inset* and *B*, *Inset*, 2 cm.)

Downloaded by guest on January 7, 2022

The TGA curve of a typical PEARL membrane is shown in Fig. 2*F*, where the remaining mass indicates the nanoparticle loading, information that is used in determining adsorption in Fig. 3. In our studies of various shapes and sizes of the PEARL membrane, the coating consistently represents 5 to 10% of the structure mass, underscoring that only a very small degree of coating is needed to transform cellulose into an effective remediation tool.

The linear isotherms displayed in Fig. 2*G* reveal the surface area of the nanoparticles alone, cellulose alone, and the nanocomposite structure. The Brunauer–Emmett–Teller (BET) surface areas are 179.5, 5.2, and 12.0 m^2/g, respectively (*SI Appendix*, Table S1). After surface area analysis, the same samples were estimated to have a nanoparticle loading of 6.5% with TGA.

Using a linear combination of the surface areas, we would then expect the nanocomposite to have a surface area of 16.5 m^2/g. This theoretical result is close to our experimental value of 12.0 m^2/g and suggests that only some of the loaded nanoparticles are not accessible to the surface. In short, the characterization shows most nanoparticles in the system comprise a thin surface coating that is actively involved in sorption.

The linear isotherm plot can also be used to show how the membrane takes on the characteristics of the nanostructures. As shown in Fig. 2*G*, the PEARL membrane and the nanoparticles have similar hysteresis loops, which suggests analogous porosity in the mesoporous (2- to 50-nm) region. This mesoporosity comes from small intrinsic agglomeration of nanoparticles. The cellulose itself has a small degree of porosity in this region as well, but based on the isotherm analysis, this contribution is little compared with that of the nanoparticles. Overall, we observe that the synthesis process allows cellulose to take on the characteristics of the tailored nanostructures.

PEARL Membrane Performance: Efficient Phosphate Recovery. Adsorption and desorption studies were performed to understand how the PEARL membrane interacts with phosphate. As shown in Fig. 3*A*, a comparable dose of MNS alone or anchored on the cellulose membrane adsorbs 98% of phosphate in a 10-mg P/L sample. The nanocomposite, however, avoids any additional centrifugation, magnetic separation, or filtration steps, making the PEARL membrane a more efficient and easy to use approach. Moreover, this comparison underscores that the majority of the nanostructures are actively involved in binding when anchored on a membrane.

The sponge itself does not participate in phosphate sequestration, so mechanism characterization can focus on nanostructures alone. Additionally, greater than 99% remediation is observed in Fig. 3*B* by using multiple, short passes (between one and four treatment steps).

The composite material itself is very stable, and nanoparticles are anchored by strong chemical affinity between MNS surface hydroxyl groups and cellulose surface moieties. There is no visible change to the solution after remediation. Across multiple experiments with various conditions, we observe iron concentrations in solutions after treatment that correspond to a 0.2% mass loss of nanocomposite (*SI Appendix*, Table S2). This result confirms that the hydrogen bonding that holds the nanoparticles to the cellulose is strong and makes a robust composite material that can be used over multiple cycles.

Fig. 3*C* shows the pH dependence of adsorption. There are small changes to the pH of the solution with treatment, as illustrated in *SI Appendix*, Fig. S4. The mechanism of desorption can be explained by the change in pH and surface charge of the material. OH^- competes with PO_4^{3-} at basic conditions, and the surface potential of the iron oxide changes from positive to negative as shown in *SI Appendix*, Fig. S5 and in the literature (23). The pH dependence can be exploited for desorption.

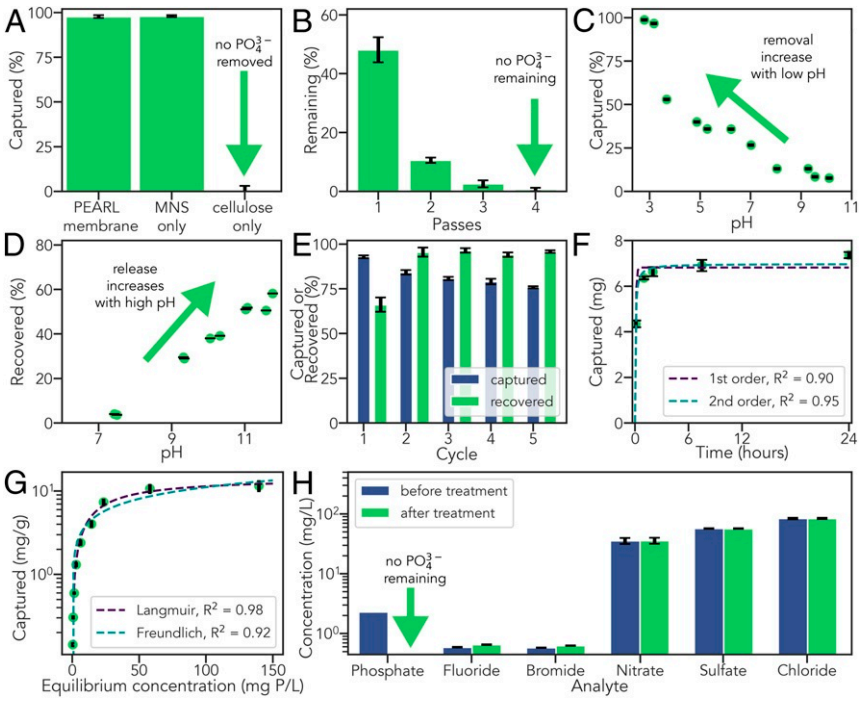


Fig. 3. (*A*) A control study demonstrates that the MNS are the sole contributors to the performance of the PEARL membrane. (*B*) After multiple treatments, more than 99% of phosphate can be captured. (*C*) Removal is pH dependent, so phosphate can be (*D*) recovered using basic conditions. (*E*) The PEARL membrane can be used for multiple cycles, and after the first cycle, 95% of phosphate can be recovered. (*F*) Kinetic study of phosphate adsorption. (*G*) Isotherm study of phosphate adsorption. (*H*) Tests on POTW effluent samples show selective binding.

Downloaded by guest on January 7, 2022

After a PEARL membrane was used for phosphate removal, it was transferred to an aqueous solution of varying pH. As shown in Fig. 3*D*, when the conditions are basic, the phosphate can be captured for reuse.

Here, up to 58% of the phosphate removed from the solution was recovered. As shown in *SI Appendix*, Fig. S6, up to 74% of the phosphate can be recovered when the time is extended. Nonetheless, this result suggests that a small fraction of the phosphate is irrevocably bonded to the nanoparticles, an observation that correlates well with electronic-state studies in *The Origin of the PEARL Membrane Performance*. At extremely acidic or basic conditions, the nanomaterials are liable to breakdown. Ideal sequestration occurs at acidic conditions (pH = 3 to 6) and release at basic conditions (pH = 8 to 11).

Because this technology is pH dependent, it can be reused for multiple cycles. Fig. 3*E* shows adsorption behavior for the first five cycles (data are also listed in *SI Appendix*, Table S3). In this test, a PEARL membrane was moved between acidic solutions containing approximately 10 mg of P/L to basic solutions. In the first cycle, 93% of the phosphate was removed. In subsequent cycles, the performance slightly decreases, which can be attributed to residual basic solution being transferred as the membrane is cycled. Ten cycles are shown in *SI Appendix*, Fig. S7, where the pH was adjusted after each transfer; the performance is consistent across cycles.

The recovery results in Fig. 3*E* show the same behavior as described in Fig. 3*D* initially. However, after the first cycle, 95% of the phosphate can be recovered. These data suggest that after some initial preconditioning of the nanomaterials, the system reaches an equilibrium state in which ions can be more easily removed and recovered. Exceptional performance in nutrient recovery makes this nanocomposite a promising tool for phosphate remediation.

To understand the kinetics of sorption, phosphate adsorption on the membrane was stopped at various stages between 5 min and 24 h. As shown in Fig. 3*F*, although we see a slight increase in adsorption over a longer time horizon, after the first hour, the majority of the phosphate has been removed. Moreover, even within the first 5 min many anions have been recovered from solution. The short reaction times further highlight the technological relevance of the PEARL membrane.

These data were fit using first- and second-order models as shown in Eqs. **1** and **2**, where q_e is the amount of phosphate adsorbed, K_1 and K_2 are rate constants, and t is time:

$$q_t = q_e(1 - e^{-K_1 t}) \quad [1]$$

$$q_t = \frac{K_2 q_e^2 t}{1 + K_2 q_e t}. \quad [2]$$

The results in Fig. 3*F* show better agreement with the second-order results. Fit parameters are listed in *SI Appendix*, Table S4, and the agreement with the second-order model suggests that chemisorption contributes to the binding mechanism.

Sorption data can be fit with equilibrium isotherm models for more insight into interaction between nanoparticles and analytes. Langmuir describes a monolayer of noninteracting analytes that adsorb onto active sites. Alternatively, the Freundlich model, based on experimental results, is often more applicable when multiple types of sorption sites exist in parallel with different free energies and site abundances. The data were fit with the Langmuir (Eq. **3**) and Freundlich (Eq. **4**) models:

$$q_e = \frac{q_{max} K_L C_e}{1 + K_L C_e} \quad [3]$$

$$q_e = K_F C_e^{1/n}, \quad [4]$$

where C_e is the equilibrium concentration after treatment, q_e is the amount adsorbed, K_L is the Langmuir constant related to binding affinity, q_{max} represents the number of surface sites, K_F is the Freundlich capacity factor, and n is the Freundlich exponent. The sorption data in Fig. 3*G* suggest that the Langmuir isotherm may be more appropriate at this concentration range. Fit parameters are listed in *SI Appendix*, Table S5.

Other factors can also influence performance, such as the addition of other ions changing the ionic strength of the material. Given the complex interplay between pH, ionic strength, interaction time, and concentrations of various competing ions, the performance of nanomaterials will be hindered or enhanced by the introduction of salts (33, 34). *SI Appendix*, Fig. S8 shows remediation results with solutions that have higher ionic strengths.

The selectivity of the PEARL membrane was further tested with real water samples from the Metropolitan Water Reclamation District of Greater Chicago (MWRD), operator of seven treatment plants, including one of the largest in the world. Effluent samples taken after secondary treatment from this publicly owned treatment works (POTW) were tested in a batch setup with the PEARL membrane.

These water samples have many dissolved ions that could potentially interfere with nanoparticle–phosphate binding. The samples had approximately 2 mg of PO_4^{3-}/L, and the PEARL membrane could nonetheless reduce the phosphate concentration below 20 μg of PO_4^{3-}/L (>99% remediation), without adsorbing other anions as shown in Fig. 3*H*. We tested up to 1 L of sample bringing the concentration from 2.3 mg of PO_4^{3-}/L to below 20 μg of PO_4^{3-}/L (>99% remediation), illustrating the possibility of scaling this method beyond the bench top (*SI Appendix*, Fig. S9).

Crucially, the PEARL membrane did not alter the concentration of nitrates. As both nutrients contribute to hypereutrophication and the ratio of N to P is essential for maintaining ecosystem homeostasis, it is important to be able to capture anions independently.

The Origin of the PEARL Membrane Performance. X-ray photoelectron spectroscopy (XPS) is a powerful tool to be able to probe the electronic structure of materials. Because this technique provides optimal interpretability with materials of flat, uniform geometry, nanoparticles without cellulose were investigated using this method. Three samples were prepared: 1) MNS, MNS alone; 2) adsorb, MNS after adsorbing phosphate; and (3) desorb, MNS after phosphate has been desorbed with an NaOH solution. As a control, KH_2PO_4: potassium phosphate monobasic and NaOH: sodium hydroxide were also tested. For reference, the carbon peak is shown in *SI Appendix*, Fig. S10.

As shown in Fig. 4*A*, comparing the MNS-only sample and the adsorption sample, we observe a shift in iron toward a more oxidized state, which is expected if iron atoms bind with phosphate (35). After the phosphate is removed, the iron peak shifts to a slightly lower binding energy than its original state. This suggests an irrecoverable change to the material after the first cycle. In Fig. 3*E*, we observed higher phosphate recovery efficiency (95%) of the PEARL membrane after the first cycle, which correlates with this XPS result.

The changes to the phosphate peak (Fig. 4*B*) correspond with the changes to the iron peak. Compared with pure KH_2PO_4, the phosphorus moves to slightly lower energy when adsorbed on iron. After phosphate is desorbed, there nonetheless remains a small phosphorus peak, suggesting that some phosphorus cannot be removed with a basic solution. This phosphorus peak has a lower binding energy, which is a shift toward binding energies of phosphide compounds. This suggests that the phosphorus that is not recoverable has some degree of bonding that is more characteristic of phosphide complexes. The signals from the oxygen peak (Fig. 4*C*) are as expected summations of the Fe_3O_4, NaOH, and KH_2PO_4 signals.

Downloaded by guest on January 7, 2022

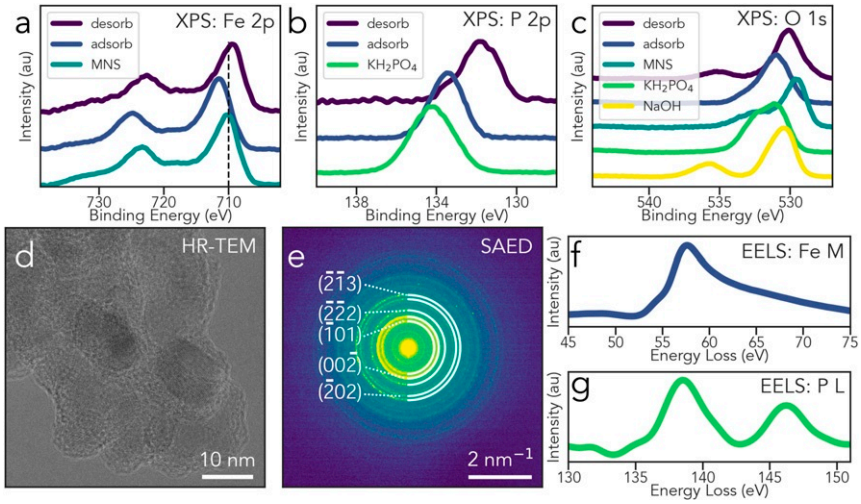


Fig. 4. XPS curves showing (*A*) iron (2p orbital), (*B*) phosphorus (2p orbital), and (*C*) oxygen (1s orbital) electronic state of nanostructures before interaction with phosphate (MNS), after adsorption (adsorb), and after desorption (desorb). NaOH and KH_2PO_4 are shown as reference. The line in *A* is added to aid the eye. (*D*) The high-resolution TEM (HR-TEM) image and the corresponding (*E*) SAED pattern show MNS structure and composition. (*F*) Iron (M edge or 3p orbital) and (*G*) phosphorus (L edge or 2p orbital) EELS edges confirm binding on the nanoscale.

One limitation of XPS is that the spot size is on the micrometer scale, while the binding mechanism of interest occurs on the molecular scale. Scanning transmission electron microscopy (STEM) is a promising correlative technique, as it collects chemical and physical information about the sample on the atomic and nanoscales. Fig. 4*D* shows a typical area of interest for study. The selected area electron diffraction (SAED) pattern from that region (Fig. 4*E*) confirms the Fe_3O_4 structure.

Such an area's electronic state can also be probed on the nanoscale with electron energy loss spectroscopy (EELS). Given the intrinsic challenges in observing phosphorus's EELS edge and the beam sensitivity of nutrients, it can be difficult to characterize this system (36). To gain sufficient spatial information and signal to noise from a low-dose acquisition, we employed a direct electron detector to acquire EELS spectra.

In this study, a sample of nanoparticles after phosphate binding was studied (adsorb sample from XPS) with EELS. As shown in Fig. 4*F*, we observed the iron M edge (3p orbital) from the nanoparticles. Despite the significant challenges in characterizing phosphorus, we were able to observe its L edge (2p orbital) as shown in Fig. 4*G*. This edge corresponds with other studies of iron oxide–phosphate complexes (37).

In addition to successfully confirming iron–phosphate bonding on the nanoscale, we can map the phosphorus distribution in the sample as shown in *SI Appendix*, Fig. S11. There are some subtle differences between the dark field, Fe, and P maps, which are worth future study to truly understand the binding mechanism.

Summary and Outlook

Phosphate pollution, as with many environmental challenges, requires a remediation strategy that is effective, economically viable, and environmentally friendly. When developing a tool to sequester phosphate, the PEARL membrane, as with its predecessor the OHM sponge, was designed with these practical priorities in mind.

This work demonstrates how the PEARL membrane can effectively remove up to 99% of phosphate from aqueous media. We tested this material on complex POTW effluent samples to show the practicality and selectivity of this technology. Moreover, we can reuse the PEARL membrane for multiple cycles to recover, not just eliminate, phosphate. The PEARL membrane is especially effective in the single-digit mg of P/L concentration range where conventional technologies fall short, which would make it a useful complementary remediation tool for point sources and natural systems with high nutrient concentrations (11–13).

Given the promising performance of the PEARL membrane, this work demonstrates that this technology is ready for scale-up and further development. In addition to maintaining the fidelity of the material, there are additional challenges in further developing a membrane such as mass transport, biofouling, and competition from pollutants with orders of magnitude higher concentration. There are many promising solutions being developed that could help alleviate these problems, such as reactors to facilitate increased residence time for nanoparticle–pollutant interactions, chemical and physical cleaning of membranes, addition of antimicrobial nanoparticles on the platform membrane, and multistage treatment systems (38–40).

More broadly, this study serves as a demonstration of how a nanocomposite can bridge the gap between nanostructure solution and the scope of environmental problems. This unique approach transforms a cheap, biocompatible, readily available porous material into an effective, deployable technology. Our approach makes efficient use of materials, as it requires only a thin (5 to 10 wt %) coating of nanomaterials applied using water-based and scalable processes. Because this platform technology is quite tunable, a similar cost-effective and sustainable approach can be employed to address other stewardship challenges.

Experimental

PEARL Membrane Synthesis. Iron precursors and NaOH were bought from Sigma-Aldrich and used as received. Iron oxide (Fe_3O_4) nanoparticles were prepared using a batch coprecipitation method. $FeCl_2{\cdot}4H_2O$ and $FeCl_3{\cdot}6H_2O$ were dissolved in deionized (DI) water with a 1:2 ratio. Excess NaOH was separately dissolved in DI water and subsequently added to the iron solution. Nanoparticles were washed thoroughly with magnetic separation followed by decanting until the pH of the slurry was stable.

Cellulose sponges were acquired from Thermo Fischer Scientific. Sponges were cut to size with a razor blade. After thorough washing with DI water, they were dip coated with an aqueous slurry of nanoparticles and then dried at 60 °C in a box furnace. The membrane was washed in DI water until the coating was stable and then returned to the box furnace for drying. The PEARL membrane was allowed to cool to ambient temperature.

Downloaded by guest on January 7, 2022

Adsorption Studies. Phosphate samples were made by dissolving potassium phosphate monobasic (Sigma-Aldrich) in DI water. Sorption was tested in 30-mL batch processes using falcon tubes. Adsorbents were added to the falcon tubes and placed on an orbital shaker for test duration. All experiments were done in triplicate. Unless otherwise noted, two PEARL membranes were used for each experiment. Each PEARL membrane weighs approximately 135 mg with 5 to 10 wt % active material. Initial concentrations of phosphate solutions are 10 mg of P/L except where noted. Adsorption and desorption experiments were 1 h long unless otherwise noted. In the multipass test (Fig. 3*B*), only one membrane was used for each pass for a shorter (45-min) adsorption treatment with a higher concentration (20 mg P/L). For the cycle test (Fig. 3*E*), both the adsorption and desorption times were only 20 min. To show the impact of ionic strength, additional NaCl (ACS reagent; Thermo Fisher Scientific) was added.

The Orion Star A111 Benchtop pH Meter (Thermo Fisher Scientific) was used for pH determination calibrated with buffers at pH 4, 7, and 10 (Thermo Fisher Scientific). Adjusting of pH was done with HCl (36.5 to 38.0%; Thermo Fisher Scientific) and NaOH (Sigma-Aldrich) solutions.

Samples from Terrence J. O'Brien, water reclamation plant (WRP), Skokie, IL were tested after secondary treatment (MWRD POTW). These complex aqueous samples have a number of dissolved ions that compete against phosphate for binding.

Phosphate Concentration Determination. Quantification of P and Fe was accomplished using inductively coupled plasma optical emission spectroscopy (ICP-OES) of acid-digested samples. Samples were digested in concentrated trace nitric acid (>69%; Thermo Fisher Scientific) and placed at 60 °C for at least 30 min. Ultrapure H_2O (18.2 MΩ·cm) was added to produce a final solution of 3.0% (vol/vol) nitric acid in a total sample volume of 10 mL. Quantitative standards ranging from 160 to 0.05 μg/g P or Fe were made using a 1,000 μg/mL P or Fe standard (Inorganic Ventures) in 3% (vol/vol) nitric acid. *SI Appendix*, Table S6 lists the concentrations used for each experiment.

ICP-OES was performed on a computer-controlled (QTEGRA software) Thermo iCap7600 ICP-OES (Thermo Fisher Scientific) operating in axial view (phosphorus) and radial view (iron) and equipped with a CETAC 520 autosampler. Each sample was acquired using a 5-s visible exposure time and a 15-s ultraviolet (UV) exposure time, running three replicates. The spectral lines selected for analysis were P = 177.495 nm and Fe = 259.940 nm.

Ion chromatography (IC) was performed using a Thermo Scientific Dionex ICS-5000+ equipped with a Dionex AS-DV autosampler and using a Dionex IonPac AS22 column (product no. 064141; Thermo Scientific). The analysis was run using an eluent of 4.5 mM sodium carbonate and 1.4 mM sodium bicarbonate (product no. 063965; Thermo Scientific) and a Dionex AERS 500 Carbonate 4-mm Electrolutically Regenerated Suppressor (product no. 085029; Thermo Scientific). A mixed elemental standard containing 1,000 μg/mL each F^-, Cl^-, Br^-, $NO_2{}^-$, $NO_3{}^-$, PO_4^{3-}, and SO_4^{2-} (IV-STOCK-59 from Inorganic Ventures) was used to make quantitative standards consisting of 25, 5, 1, 0.5, 0.1, and 0.5 μg/mL each anion in ultrapure H_2O.

Recovery data were collected with ion chromatography instead of ICP-OES. When more basic conditions were used, the IC data showed nonstandard peaks and drifting of expected peaks, which suggest breakdown of the PEARL membrane and phosphate as shown in *SI Appendix*, Fig. S12. This information is not accessible in a typical ICP-OES measurement, where samples are digested. Results were qualitatively confirmed with the ascorbic acid method as recommended by the Environmental Protection Agency (EPA) (41).

Electron Microscopy. Cross-sectional samples for scanning electron microscopy and STEM were prepared by embedding membranes in resin and cutting with the Leica UC7/FC7 Cryo-Ultramicrotome. Nanostructures were prepared for transmission electron microscopy (TEM) analysis by drop casting on a lacey carbon grid.

Images were collected with the Concentric Backscattered Detector on the scanning electron microscopy (SEM) FEI Quanta 650 operated at 20 kV in low-vacuum mode to minimize charging artifacts. Scanning electron microscopy images of the sectioned samples were acquired with the Retractable Backscattered Electron Detector on the JEOL 7900FLV operated at 5 kV in low-vacuum mode. The image was taken in backscatter mode in order to emphasize the compositional contrast of the material.

STEM images of the sectioned samples were acquired using a Hitachi HD-2300 operated at 200 kV. EDS was collected using a dual-detector system. The results were summed across 120 frames.

TEM imaging of the nanoparticles was performed at 300 kV with the JEOL ARM300F GrandARM. STEM imaging of the nanoparticles was acquired on the JEOL ARM200CF Aberration-Corrected TEM operated at 200 kV. EELS data were taken in EELS acquisition mode with a Gatan K2 Summit direct electron detector mounted on a JEOL ARM200CF. The instrument was operated at 200 kV in STEM mode with a camera length of 2 cm. The convergence angle of the probe was 27 mrad, and the spectrometer was operated with a dispersion of 0.1 eV per channel.

EELS spectra were aligned to the zero-loss peak, and background of edges was subtracted using a power law fit algorithm. Phosphate ions are strongly susceptible to beam damage; thus, a noisy EELS dataset was acquired, and nearest neighbor averaging in real space and Gaussian smoothing in energy space were used to boost signal to noise. To keep our dispersion low, we quantified iron using its strong M peak. It is well known that phosphorus is a difficult element to quantify due to the overlap in its L (2p orbital) signal (132 eV) with the plasmon edge (36). Nonetheless, the L edge was chosen for its superior signal to noise over other phosphorus edges, and its shape could be revealed with proper background subtraction.

Surface Area Determination. N_2 adsorption and desorption isotherms were obtained at 77 K by a 3Flex analyzer (Micromeritics). Measurements were performed on nanoparticles alone, cellulose alone, and the composite structure. Pore characteristics were calculated using a cylindrical porous oxide surface area density-functional theory (DFT) model for monolayer adsorption. Surface area was determined using the BET method.

TGA. TGA was conducted using a Mettler Toledo combined TGA/differential scanning calorimetry (DSC) 3+ to confirm nanoparticle mass loading and to observe the effects of the nanoparticle coating on the thermal properties of the sponge. TGA experiments used a temperature profile from room temperature to 800 °C. The temperature was held at 40 °C for 3 min, then increased to 150 °C at 10 °C/min to capture the loss of water weight, and subsequently increased to 800 °C at 20 °C/min, capturing the total combustion of the sponge and allowing for determination of the mass of the iron oxide coating. A similar process was employed using a conventional furnace and bulk sponges. Tests were performed on typical PEARL membranes of various sizes.

XPS. XPS was conducted using a Thermo Scientific ESCALAB 250Xi system with charge referenced to adventitious carbon 1s orbital, carbon–carbon peak at 284.8 eV. Samples were prepared for analysis by vacuum drying to avoid any change in oxidation state that can occur with heating.

Downloaded by guest on January 7, 2022

X-Ray Powder Diffraction. X-ray diffraction measurements were taken on powder samples using Rigaku SmartLab with Cu-Kα (copper 2p orbital) radiation (λ = 1.5418 Å). Patterns were background subtracted. Results were plotted against patterns simulated in Vesta from a computed structure (42).

Surface Charge. A Malvern Zetasizer Nano ZS90 with a 633-nm laser was used to conduct the zeta potential measurements. Measurements were performed in a clear disposable cuvette at room temperature.

Data Availability. All study data are included in the article and/or *SI Appendix*.

ACKNOWLEDGMENTS. The research related to oxide nanostructured architecture is supported by the NSF Grant DMR-1929356 (Ceramics Program, Program Manager: Dr. Lynnette Madsen). This work made use of the Electron Probe Instrumentation Center (EPIC), BioCryo, and Keck-II facilities of Northwestern University Atomic and Nanoscale Characterization Experimental (NU*ANCE*) Center, which has received support from the Soft and Hybrid Nanotechnology Experimental (SHyNE) Resource (NSF Grant ECCS-2025633), the International Institute of Nanotechnology (IIN), and Northwestern's Materials Research Science and Engineering Center (MRSEC) program (NSF Grant DMR-1720139). This work made use of the Jerome B. Cohen X-Ray Diffraction Facility supported by the MRSEC program (NSF Grant DMR-1720139) at the Materials Research Center of Northwestern University and the SHyNE Resource (NSF Grant ECCS-2025633). Elemental analysis was performed at the Northwestern University Quantitative Bio-element Imaging Center. Nitrogen adsorption isotherm analysis was performed at the Northwestern Reactor Engineering and Catalyst Testing core facility. S.M.R. acknowledges support from the American Membrane Technology Association and the National Water Research Institute. We thank Tirzah Abbott, Eric W. Roth, Charlene Wilke, Dr. Reiner Bleher, Dr. Paul J. M. Smeets, Dr. Akshay A. Murthy, Dr. Neil M. Schweitzer, Rebecca Sponenburg, and Christopher Metellus for their contributions. We acknowledge support from MWRD Commissioner Debra Shore, Tom Kunetz, Dr. Kuldip Kumar, and the Terence J. O'Brien WRP's Maintenance and Operation Staff.

1. J. Rosen, Humanity is flushing away one of life's essential elements. The Atlantic, 8 February, 2021. https://www.theatlantic.com/science/archive/2021/02/phosphorus-pollution-fertilizer/617937/.
2. M. F. Chislock, E. Doster, R. Zitomer, A. E. Wilson, Eutrophication: Causes, consequences, and controls in aquatic ecosystems. *Nature Education Knowledge Project* **4**, 10 (2013).
3. C. Le, Y. Zha, Y. Li, D. Sun, H. Lu, B. Yin, Eutrophication of lake waters in China: Cost, causes, and control. *Environ. Manag.* **45**, 662–668 (2010).
4. J. N. Pretty *et al.*, Environmental costs of freshwater eutrophication in England and Wales. *Environ. Sci. Technol.* **37**, 201–208 (2003).
5. D. Egan, *The Death and Life of the Great Lakes* (W. W. Norton and Company, 2018).
6. V. Smith, D. Schindler, Eutrophication science: Where do we go from here? *Trends Ecol. Evol.* **24**, 201–207 (2009).
7. D. J. Conley *et al.*, Ecology—controlling eutrophication, nitrogen and phosphorus. *Science* **323**, 1014–1015 (2009).
8. Y. P. Khare, G. M. Naja, R. Paudel, C. J. Martinez, A watershed scale assessment of phosphorus remediation strategies for achieving water quality restoration targets in the western Everglades. *Ecol. Eng.* **143**, 105663 (2020).
9. E. Sinha, A. M. Michalak, V. Balaji, Eutrophication will increase during the 21st century as a result of precipitation changes. *Science* **357**, 405–408 (2017).
10. D. Tonini, H. G. M. Saveyn, D. Huygens, Environmental and health co-benefits for advanced phosphorus recovery. *Nat. Sustain.* **2**, 1051–1061 (2019).
11. E. Desmidt *et al.*, Global phosphorus scarcity and full-scale p-recovery techniques: A review. *Crit. Rev. Environ. Sci. Technol.* **45**, 336–384 (2015).
12. M. C. Chrispim, M. Scholz, M. Antunes Nolasco, Phosphorus recovery from municipal wastewater treatment: Critical review of challenges and opportunities for developing countries. *J. Environ. Manag.* **248**, 109268 (2019).
13. C. M. Mehta, W. O. Khunjar, V. Nguyen, S. Tait, D. J. Batstone, Technologies to recover nutrients from waste streams: A critical review. *Crit. Rev. Environ. Sci. Technol.* **45**, 385–427 (2015).
14. X. Zhao, K. Kumar, M. A. Gross, T. E. Kunetz, Z. Wen, Evaluation of revolving algae biofilm reactors for nutrients and metals removal from sludge thickening supernatant in a municipal wastewater treatment facility. *Water Res.* **143**, 467–478 (2018).
15. D. J. Ballantine, C. C. Tanner, Substrate and filter materials to enhance phosphorus removal in constructed wetlands treating diffuse farm runoff: A review. *N. Z. J. Agric. Res.* **53**, 71–95 (2010).
16. S. Tyagi, D. Rawtani, N. Khatri, M. Tharmavaram, Strategies for nitrate removal from aqueous environment using nanotechnology: A review. *J. Water Proc. Eng.* **21**, 84–95 (2018).
17. Y. Wu *et al.*, Environmental remediation of heavy metal ions by novel-nanomaterials: A review. *Environ. Pollut.* **246**, 608–620 (2019).
18. A. K. Mishra, C. M. Hussain, S. B. Mishra, *Nanomaterials for Water Remediation* (Walter de Gruyter GmbH and Co KG, 2020).
19. S. Ahmed *et al.*, Ethylene glycol-assisted fabrication and superb adsorption capacity of hierarchical porous flower-like magnesium oxide microspheres for phosphate. *Inorg. Chem. Front.* **6**, 1952 (2019).
20. J. He *et al.*, Ce(III) nanocomposites by partial thermal decomposition of Ce-MOF for effective phosphate adsorption in a wide pH range. *Chem. Eng. J.* **379**, 122431 (2020).
21. X. Min *et al.*, Ultra-high capacity of lanthanum-doped uio-66 for phosphate capture: Unusual doping of lanthanum by the reduction of coordination number. *Chem. Eng. J.* **358**, 321–330 (2019).
22. Z. Ajmal *et al.*, Phosphate removal from aqueous solution using iron oxides: Adsorption, desorption and regeneration characteristics. *J. Colloid Interf. Sci.* **528**, 145–155 (2018).
23. D. Jiang, Y. Amano, M. Machida, Removal and recovery of phosphate from water by a magnetic Fe_3O_4@ASC adsorbent. *J. Environ. Chem. Eng.* **5**, 4229–4238 (2017).
24. S. Y. Yoon *et al.*, Kinetic, equilibrium and thermodynamic studies for phosphate adsorption to magnetic iron oxide nanoparticles. *Chem. Eng. J.* **236**, 341–347 (2014).
25. J. Choi, J. Chung, W. Lee, J. O. Kim, Phosphorous adsorption on synthesized magnetite in wastewater. *J. Ind. Eng. Chem.* **34**, 198–203 (2016).
26. D. A. Almasri, N. B. Saleh, M. A. Atieh, G. McKay, S. Ahzi, Adsorption of phosphate on iron oxide doped halloysite nanotubes. *Sci. Rep.* **9**, 1–13 (2019).
27. V. Nandwana *et al.*, OHM sponge: A versatile, efficient, and ecofriendly environmental remediation platform. *Ind. Eng. Chem. Res.* **59**, 10945–10954 (2020).
28. V. Nandwana, V. P. Dravid, "Oleophilic hydrophobic magnetic sponge." US Patent 62/788,347 (2019).
29. A. Zach-Maor, R. Semiat, H. Shemer, Synthesis, performance, and modeling of immobilized nano-sized magnetite layer for phosphate removal. *J. Colloid Interf. Sci.* **357**, 440–446 (2011).
30. K. W. Jung, K. H. Ahn, Fabrication of porosity-enhanced MgO/biochar for removal of phosphate from aqueous solution: Application of a novel combined electrochemical modification method. *Bioresour. Technol.* **200**, 1029–1032 (2016).
31. T. Sheela, Y. A. Nayaka, R. Viswanatha, S. Basavanna, T. G. Venkatesha, Kinetics and thermodynamics studies on the adsorption of Zn(II), Cd(II) and Hg(II) from aqueous solution using zinc oxide nanoparticles. *Powder Technol.* **217**, 163–170 (2012).
32. P. K. Raul *et al.*, Cuo nanorods: A potential and efficient adsorbent in water purification. *RSC Adv.* **4**, 40580–40587 (2014).
33. J. Antelo, M. Avena, S. Fiol, R. Ã. LÃ^{3}pez, F. Arce, Effects of pH and ionic strength on the adsorption of phosphate and arsenate at the goethite–water interface. *J. Colloid Interf. Sci.* **285**, 476–486, 2005.
34. J. Liu, L. Wan, L. Zhang, Q. Zhou, Effect of pH, ionic strength, and temperature on the phosphate adsorption onto lanthanum-doped activated carbon fiber. *J. Colloid Interf. Sci.* **364**, 490–496 (2011).
35. T. J. Daou *et al.*, Phosphate adsorption properties of magnetite-based nanoparticles. *Chem. Mater.* **19**, 4494–4505 (2007).
36. A. A. Sousa, R. D. Leapman, Development and application of stem for the biological sciences. *Ultramicroscopy* **123**, 38–49 (2012).
37. S. Miao *et al.*, Local electronic structure of olivine phases of lixfepo4. *J. Phys. Chem.* **111**, 4242–4247 (2007).
38. R. Kumar, P. Pal, A membrane-integrated advanced scheme for treatment of industrial wastewater: Dynamic modeling towards scale up. *Chemosphere* **92**, 1375–1382 (2013).
39. F. Meng *et al.*, Fouling in membrane bioreactors: An updated review. *Water Res.* **114**, 151–180 (2017).
40. G. E. Imoberdorf, H. A. Irazoqui, O. M. Alfano, A. E. Cassano, Scaling-up from first principles of a photocatalytic reactor for air pollution remediation. *Chem. Eng. Sci.* **62**, 793–804 (2007).
41. US Environmental Protection Agency, Method 365.3: Phosphorous, all forms (colorimetric, ascorbic acid, two reagent) (1978). https://www.epa.gov/sites/production/files/2015-08/documents/method_365-3_1978.pdf. Accessed 8 February 2021.
42. K. Persson, Materials data on Fe3O4 (SG:227) by materials project (2015). https://materialsproject.org/materials/mp-19306/. Accessed 8 February 2021.

Downloaded by guest on January 7, 2022